

Self-consistent modelling of a liquid metal box-type divertor with application to the Divertor Tokamak Test (DTT) facility: Li vs. Sn

Original

Self-consistent modelling of a liquid metal box-type divertor with application to the Divertor Tokamak Test (DTT) facility: Li vs. Sn / Nallo, Giuseppe Francesco; Mazzitelli, Giuseppe; Savoldi, Laura; Subba, Fabio; Zanino, Roberto. - In: NUCLEAR FUSION. - ISSN 0029-5515. - ELETTRONICO. - (2019). [10.1088/1741-4326/ab145b]

Availability:

This version is available at: 11583/2729979 since: 2019-04-04T11:38:54Z

Publisher:

IOPScience

Published

DOI:10.1088/1741-4326/ab145b

Terms of use:

This article is made available under terms and conditions as specified in the corresponding bibliographic description in the repository

Publisher copyright

IOP postprint/Author's Accepted Manuscript

"This is the accepted manuscript version of an article accepted for publication in NUCLEAR FUSION. IOP Publishing Ltd is not responsible for any errors or omissions in this version of the manuscript or any version derived from it. The Version of Record is available online at <http://dx.doi.org/10.1088/1741-4326/ab145b>

(Article begins on next page)

Self-consistent modelling of a liquid metal box-type divertor with application to the Divertor Tokamak Test (DTT) facility: Li vs. Sn

G. F. Nallo^a, G. Mazzitelli^b, L. Savoldi^a, F. Subba^a, R. Zanino^{a*}

^aNEMO group, Dipartimento Energia, Politecnico di Torino, Torino, Italy

^bENEA, Fusion and Technologies for Nuclear Safety Department, C.R.Frascati, C.P.65-00044Frascati, Rome, Italy

*Corresponding author

In the present work a model for a liquid metal (LM) box-type divertor is presented, aimed at including the most relevant aspects of its rich physics, as well as some engineering elements. Given the upstream plasma conditions and for a fixed divertor geometry, the model self-consistently evaluates the plasma heat and particle flux on the LM surface, the thermodynamic state of the metal (liquid and vapor) in the divertor boxes and the temperature distribution in the solid walls. The model is then applied to the Divertor Tokamak Test (DTT) facility, which is currently being designed in Italy, comparing Li and Sn as possible LM choices, in terms of operating temperatures and of metal vapor flux from the divertor box system towards the main plasma chamber.

Keywords: Nuclear fusion reactors, Tokamak, Power Exhaust, Liquid Metal Divertor, DTT

1. Introduction

Liquid metals (LMs) have been long recognized as having the potential of providing a reliable solution for the power exhaust problem in fusion reactors, which is one of the most significant milestones towards the production of the first kWh from the fusion energy source [1].

In the 90s, the idea of an LM divertor based on a Capillary-Porous Structure (CPS) coating was proposed ([2],[3]). From that moment on, a series of fundamental physics studies [4], [5] and experimental campaigns [6],[7],[8],[9],[10] were started worldwide. Experiments showed that the use of Li in plasma discharges is beneficial in terms of improved confinement, plasma purity, low recycling and consequently enhanced reactor performance. Moreover, Mirnov et al. [11] showed that Li could be effectively used as an impurity to cool the SOL plasma. The steady state power handling capability of actively cooled Li-filled CPS targets has been experimentally tested for small mock-ups up to 25 MW/m² [12]. During these experiments, as well as during short power excursions to 50 MW/m², no damage to the CPS nor ejection of LM droplets has been observed. Recent modeling in [13] suggests that steady state heat fluxes as large as 100 MW/m² can be tolerated without damage. These figures indicate a steady state power handling capability which is, in the most pessimistic condition, comparable with the one foreseen for the current solid (W) divertors [14], with the added value of significantly improved resilience to transient events.

A second class of LM divertor proposals is represented by concepts such as LiMIT [15], ACLMD [16] and others (see [17] for a thorough review). These proposals are characterized by fast LM flow, as opposed to the slow flow typical of surface replenishment via capillary forces in a CPS. This can be exploited to maintain the Li surface below ~500°C, so that significant Hydrogen retention takes place [4]. The resulting low-recycling plasma regime is characterized by superior performances and represents one of the main advantages for this divertor proposal. In this case Li acts as a pump for hydrogenic species, and therefore fuel recovery can take place by purification of the circulating LM. These concepts are very promising, even though the level of maturity in terms of robust power handling is lower with respect to slow-flow concepts [18].

In 2009 Nagayama ([19]) proposed four different LM divertor concepts, the simplest of which consisted of an LM pool contained in a so-called Evaporation Chamber (EC). To reduce the flux of Li vapor towards the main plasma chamber, the author proposed to add a Differential Chamber (DC), connected to the EC, where passive pumping of Li vapor could take place thanks to condensation. The concept was based on the evaporative cooling, i.e. on exploiting the LM latent heat of evaporation to partly exhaust the heat coming from the plasma. Independently, Ono et al. [20] proposed an LM divertor which relied on plasma cooling associated to interactions with the vapor to exhaust the plasma heat load, whereas evaporation of a liquid substrate was only considered as *extrema ratio*. Those two ideas were then combined and further developed by Goldston ([21],[22]), who proposed a new concept, called “Li vapor box divertor”, where both effects were exploited. To achieve this objective, he proposed a divertor made of a series of boxes intended to confine a large density of Li vapor in the divertor region, thereby locally enhancing plasma-Li vapor interactions. The necessary reduction of vapor flux towards the main plasma chamber (MC) was achieved by means of passive pumping of the boxes via condensation. The walls of the various chambers were coated by LM-filled CPS, and no pool was foreseen. In [23] we

proposed a vapor box divertor with an LM pool, i.e. an LM divertor inspired by the pool concept in [19], but intended to take advantage of the plasma-vapor interactions as suggested in [20], [21] and [22]. A simplified but self-consistent model featuring a 0D treatment of the metal vapor interacting with the plasma in each chamber was also presented in [23]. That model was capable of showing, at least qualitatively, the potential of the Li vapor to redistribute the plasma heat load over the chamber walls. Moreover, it was shown that passive pumping due to Li vapor condensation could reduce the main plasma chamber Li contamination. However, that simple model, being 0D, did not take into account the actual system geometry. Moreover, the very simplified treatment of plasma-vapor interactions relied on an assumed average value of the energy lost by the plasma per vapor atom interacting with it. The uncertainties concerning this value significantly affected the results.

In the present work, for the first time, a model which self-consistently evaluates the state of the vapor, of the plasma and of the divertor walls for a box-type LM divertor with a pool is presented. The model can be used to assess the influence of the particular cooling strategy employed for the divertor (coolant temperature, shape and location of the cooling channels) on the overall behavior of the system (plasma state, wall temperature, circulating LM and vapor mass flow rates), which makes it suitable for engineering applications. Moreover, the self-consistency allows to provide a fair comparison between Li and other LMs which are currently being considered for an LM divertor, such as Sn [24]. The comparison is carried out in terms of operating temperatures of both the LM and the divertor structures, as well as in terms of the impurity flux towards the main plasma chamber and of the recirculating LM flow rate. The model is applied to the Divertor Tokamak Test (DTT) facility, currently under design in Italy, which should assess alternative solutions for the power exhaust problem in future fusion reactors, including an LM divertor ([25], [26], [27]).

The paper is organized as follows: we shall first provide a description of the system at hand. The phenomenology associated to a liquid metal divertor is then briefly recalled. To explain why Li and Sn are currently considered as the best candidates for an LM divertor, their most relevant thermophysical and atomic properties are summarized. The proposed model, organized in three modules -- LM, scrape-off layer (SOL) and walls, respectively, is then discussed in some detail, with particular reference to the assumptions made in each of the three modules. The DTT operating scenario assumed for the calculations is then described. The results are finally presented and discussed, comparing the behavior of Li and Sn.

2. System description

Starting from the available CAD of the tokamak chamber [28], a tentative layout of a box-type LM divertor has been suggested for the DTT, see Figure 1: as for the conventional divertor foreseen for DTT, LM divertor is divided in 18 sectors (one for each TF coil). Each sector is further subdivided into three cassettes. The proposed geometry takes into account geometrical constraints such as the dimension of the tokamak chamber and the presence of two in-vessel copper PF coils (C1 and C4 in Figure 2) which are designed for plasma control or local field modification in the divertor region. Figure 2 also shows the most relevant dimensions of the system at hand and introduces the nomenclature which shall be used throughout the paper (IEC = Inboard Evaporation Chamber, IDC = Inboard Differential Chamber, OEC = Outboard Evaporation Chamber and ODC = Outboard Differential Chamber). As in the original Nagayama proposal [19], two chambers have been proposed for each divertor leg rather than a larger number, as proposed in [21]. A larger number of chambers might be needed in case the vapor flux towards the main plasma was excessively large, provided room and structural constraints will allow installing them.

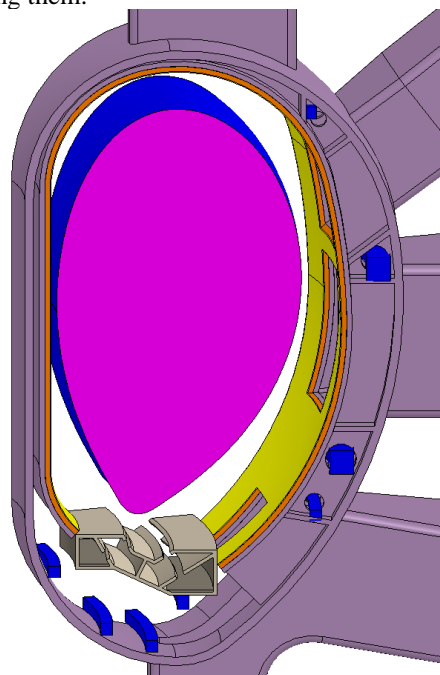


Figure 1. CAD of the proposed box-type divertor inserted in the DTT envelope [28]. Note that the structural connection of the divertor to the vacuum vessel is not shown.

Figure 2 shows a poloidal section of IEC and OEC connected to separate differential chambers, with the “interaction region” between the SOL plasma and the metal vapor highlighted in red. The position of the apertures has been chosen according to the available reference SN equilibrium for the machine [28]. The choice of the width of the apertures follows instead from a trade-off. Indeed, one should keep them as small as possible to avoid excessive vapor flux from the IDC and ODC to the main plasma. Conversely, one should design larger apertures to avoid sputtering production which would occur, should the relatively high-temperature SOL plasma touch the aperture borders. Moreover, leading edges could melt due to normally incident heat loads (on the poloidal plane) which could follow from vertical equilibrium shifts. Consequent impurities would indeed frustrate the improvement of the plasma purity which is one of the main motivations for employing an LM divertor [29]. We have therefore estimated the particle scrape-off thickness at the point where plasma enters the DCs (beginning of the zone highlighted in red in Figure 2). This has been done by estimating the particle scrape-off thickness at the outboard midplane (OMP) based on [30] and then applying an expansion factor to take into account the expansion of the field lines. The result is ~ 1 cm and therefore a conservative value of 5 cm has been adopted for the aperture width. Nevertheless, it is recognized that the limited width of the apertures is among the limitations of the proposed design. This issue can be partially addressed by more carefully shaping the “nozzle” connecting DC and MC, but a larger aperture might be unavoidable. The resulting larger amount of vapor escaping from the DC, could be mitigated by improving the cooling of the walls -thereby increasing the vapor condensation rate- or adding a further box to the divertor, compatibly with space constraints. Further optimizations of the design are left for future work.

For the time being, each cassette is designed to be independently cooled by water, passing through toroidal channels running in parallel, which are connected to manifolds at the inlet and outlet of each cassette, respectively. A total mass flow rate of 150 kg/s per cassette, at this stage equally split among the channels, should limit the coolant temperature increase to ~ 8 K even for the most loaded channels, with an inlet temperature of 393K, see below. However, it is well known that cooling tube failure resulting in water ingress in the vacuum vessel (LOCA) could lead to hydrogen explosions, in case Li is employed as an LM [31]. Based on the results of safety assessments, this kind of situation can be avoided by adopting alternative coolants such as He cooling. As an alternative, water-gas spray cooling can provide similar heat exhaust capabilities while significantly reducing the amount of water employed, thereby limiting the consequences of a component failure [32]. W has been chosen as a wall material due to its compatibility with both Li and Sn for the range of temperatures of interest for the present work [32], [33].

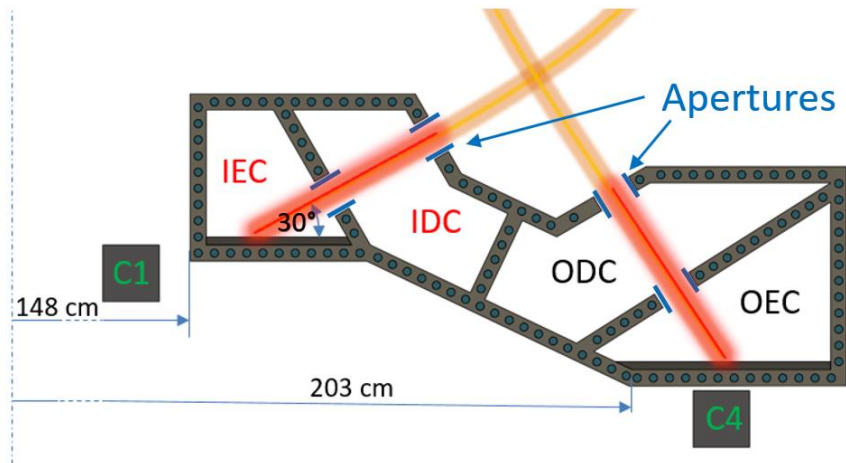


Figure 2: Cross section of the proposed DTT vapor box divertor geometry. Radial coordinates start from the symmetry axis of the torus. Interaction region between SOL plasma and metal vapor is highlighted in red.

3. Phenomenology

Metal atoms are emitted from the LM pool due to the incoming plasma heat and particle load. In particular, the heat load deposited by the Scrape-Off Layer (SOL) plasma leads to evaporation, whereas the plasma particle flux determines the emission of sputtered metal atoms ($\sim 1/3$ of the total emission) and ions ($\sim 2/3$ of the total emission) [34]. Of the emitted particles, more than 99 % are immediately redeposited due to prompt ionization [24].

To avoid confusion, the following terminology will be employed throughout the work:

- the term *vapor* indicates the atoms arising from evaporation which do not undergo prompt redeposition;
- the term *sputtered atoms* indicates the atoms arising from sputtering which do not undergo prompt redeposition;
- the term *neutral* indicates hydrogenic atoms arising from recycling at the target.

The vapour, depending on its temperature and pressure as well as on the wall temperature, can condense on the relatively cold EC wall, but it can also interact with the SOL plasma through the following processes:

- Excitation and de-excitation, leading to line radiation;
- Successive ionizations;
- Plasma entrainment effect (transport of ionized vapor towards the target, together with the hydrogenic plasma);
- Recombination of ionized vapor. If the plasma temperature is sufficiently low, this can occur before reaching the target, otherwise it occurs at the target;
- Charge-exchange between plasma ions and vapor;
- Ion-neutral friction.

These interactions lead to a cooling of the plasma (“vapor shielding” effect) and to the re-deposition of a further part of the vapor on the pool [35]. The extent of plasma cooling is quantified by the cooling function $L_z(T_e, n_e, \tau)$ ($W \cdot m^3$), which is defined by the cooling rate q_{cool} (W/m^3):

$$q_{cool} = L_z \cdot n_e \cdot n_{vap} \quad (1)$$

q_{cool} is the power per unit volume lost by the plasma due to ionization and radiation. n_e is the electron density and n_{vap} is the vapor density. L_z is a non-linear function of T_e , n_e and τ . The latter is the particle dwell time, i.e. the average time spent by an impurity atom in the plasma. Large values of τ correspond to the coronal equilibrium conditions, whereas small values lead to a non-coronal enhancement of the cooling effect [11]. The details of the interactions are determined by SOL temperature and density profiles and by the vapor density. The plasma cooling effect leads to a mitigation of the parallel heat flux reaching the pool.

The vapor not collected by the walls, nor returned to the pool, escapes the EC towards the DC, and finally escapes towards the main plasma chamber (MC). The actual state of the system -in terms of thermodynamic state of the vapor, of temperature of the chamber walls and of SOL plasma parameters- is determined by the interplay between the aforementioned phenomena. For instance, the plasma cooling effect due to interactions of the SOL plasma with the intrinsic impurities determines the heat flux reaching the pool, since part of the upstream power has been radiated. The resulting heat flux to the pool determines the LM evaporation, which is the source term for the vapor mass balance in the boxes and therefore influences the vapor density, which in turn affects the plasma cooling.

The LM condensed on the EC is assumed to be instantaneously recollected by the pool, whereas the LM condensed on the DC walls should be redirected towards the pool by means of an external recirculation circuit. This circuit could be designed to rely on the action of capillary forces to passively return the LM condensed in the DC towards the EC pool, as proposed in [36]. The vapor escaping towards the MC will instead condense on the FW. The detailed description of the engineering solution to the recollection of the condensed LM is beyond the scope of this paper. Nevertheless, it is worth mentioning that this recollected LM can be purified before being redirected to the EC, e.g. by means of a system such as the one proposed in [37].

The H retention at the pool for the proposed box-type divertor should be negligible even in case Li is employed as a LM due to the relatively large surface temperatures, as it will be explained better in section 4. Nevertheless, the temperature of the DC walls could be kept low enough to allow for H removal by the condensed LM. The proposed design does not take advantage of this possibility, meaning that active pumping of H (and He) will be required, as for conventional divertors. Details concerning the engineering of the particle exhaust (pump type and location) are beyond the scope of this work, but the interested reader can find interesting suggestions in [19].

4. Choice of the LM

Li was originally proposed as an LM to be used as a plasma-facing component due to its low Z, which makes it more tolerable, should it reach the core plasma [11]. Moreover, experiments have shown that the presence of Li in plasma discharges is responsible for an attractive improvement of the machine performance in terms of confinement and plasma purity ([11], [38]). As already mentioned in Section 3, for relatively low target temperatures (<450°C) H is retained in Li due to the formation of LiH, which can lead to an excessive accumulation of T in the chamber [39]. However, preliminary calculations in [23] showed that the temperature range of Li in both IEC and OEC pool is likely to be large enough to avoid H retention, and therefore operate in high-recycling regime.

The lower evaporation rate of Sn at the expected temperatures (~1100°C) with respect to Li, see Figure 3, leads to a lower impurity flux towards the main plasma. Moreover, it appears that Sn does not retain H significantly in any conditions [40], and it is more suitable in a water-cooled system, due to safety issues associated to Li-water interactions.

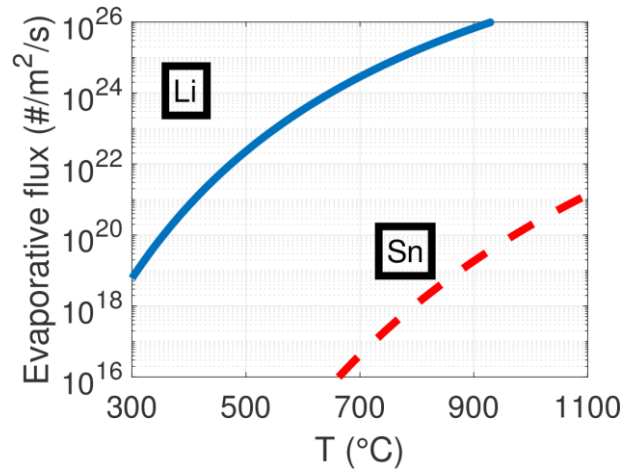


Figure 3. Evaporation flux for Li and Sn as a function of temperature, evaluated following the Hertz-Knudsen relation [41]

The cooling function L_z of Sn is also much larger than the one of Li, especially at SOL-relevant temperatures (1-100 eV), see Figure 4. This means that “vapor shielding” associated to a given amount of Sn is much more effective than the one associated to the same quantity of Li. Conversely, main plasma contamination associated to a given concentration of Sn atoms would be much more severe than the one associated with the same concentration of Li atoms. From the foregoing discussion it is clear that a quantitative and self-consistent model of the box-type divertor is required, if one wants to understand the interplay between the various above-mentioned effects.

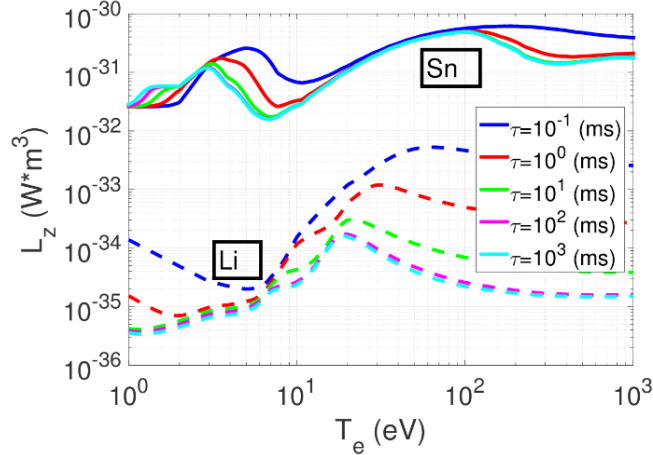


Figure 4. Plasma cooling function as a function of electron temperature and of the particle dwell time τ . Data for Li are from [42], whereas data for Sn are from [43]. Note that the cooling function includes both radiation and ionization.

Table 1 summarizes the main properties of the two LMs which have been compared in this study.

Table 1. Comparison of physical properties of Li and Sn (values from [44])

Property	Symbol (units)	Li	Sn
Charge	Z	3	50
Mass number	A (amu)	6.94	118.7
Density at melting temperature	ρ (kg/m³)	512	6990
Melting temperature	T_m (°C)	180.5	231.9
Latent heat of evaporation	ΔH_{vap} (10³ kJ/kg)	21.0	2.49
Thermal conductivity at melting temperature	$k @ T_m$ (W/m · K)	45	30
First ionization potential	E_{iz} (eV)	5.39	7.34

5. Model description

The model is composed by three coupled modules, as schematically shown in Figure 5:

1. A 0D thermodynamic model for the LM and vapor, which requires in input the power from the SOL plasma -split between the advective/conductive and the radiative channels- as well as the temperatures of the box walls and the

- total ionization rate of the vapor $\dot{N}_{iz,vap}$. The output of this module is the thermodynamic state of the Li vapor in ECs and DCs, as well as the evaporation/condensation rates and the associated heat loads on the walls;
2. A 2D FEM thermal model for the divertor walls, which requires in input the heat load on the walls and the parameters of the active cooling, as well as the heat transfer from the LM pool. The output of this module is the temperature map over the divertor structures T_{wall} ;
 3. A 1D SOL plasma model, which requires in input the upstream plasma conditions (parallel heat flux and plasma density) and the vapor density n_{vap} . The output is the 1D SOL parallel temperature, density, velocity and heat flux profiles accounting for interactions with the vapor. Consequently, it is possible to determine the power repartition among the various channels (i.e. conductive/convective and radiative), which is required for coupling with other modules.
- The three modules are explicitly coupled using under-relaxed Picard iterations, for the sake of simplicity.

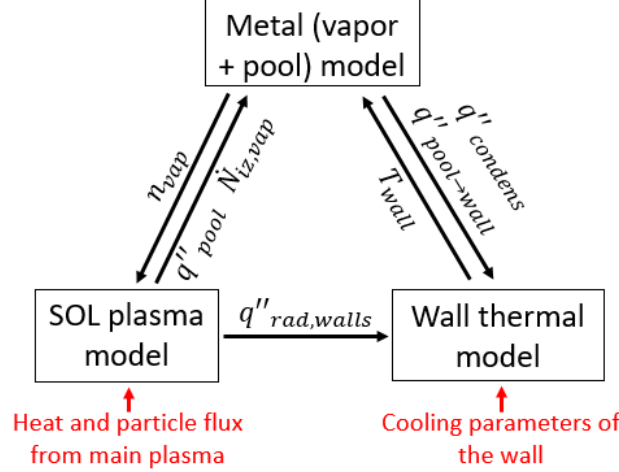


Figure 5: Schematic of the coupling strategy between the three modules of the model. The meaning of the symbols not already discussed is the following: q''_{pool} is the heat flux on the pool, $q''_{rad,walls}$ is the heat flux on the chamber walls, $q''_{pool \rightarrow walls}$ is the heat flux at the interface between the pool and the substrate, $q''_{condens}$ is the condensation heat flux.

The model assumes symmetry along the toroidal direction. While this assumption is reasonable for the SOL plasma and for the vapor, the wall -and pool- temperature will experience toroidal variations within a given sector due to the proposed cooling strategy (with the coolant temperature increasing in the toroidal direction). However, as mentioned in section 2, even for the most loaded channels the temperature increase should be $< 10K$. Applying the model to the inlet poloidal section of each sector appears therefore a reasonable approximation for the purpose of the present work.

5.1. 0D LM model

The 0D LM model evaluates the thermodynamic state of the Li liquid-vapor system within the various chambers. This model has already been presented in [23], therefore we shall only briefly report its main features here.

The model is based on mass and energy conservation within the divertor chambers. For the sake of clarity, the energy balance for the EC is schematically shown in Figure 6, where the nomenclature is as follows:

- $Q_{condens}(W)$ is the heat load associated to vapor condensation on walls;
- $Q_{noz}(W)$ is the heat load associated to the vapor flux from EC to DC;
- $Q_{entr}(W)$ is the heat load associated to the entrained Li (Sn) returning to the EC together with the plasma flow;
- $Q_{SOL}(W)$ is the amount of power carried by the SOL plasma to the metal in the EC. Of this power, an amount Q_{rad} will be radiated due to plasma-vapor interactions in the EC. A fraction $f_{rad,pool}$ of Q_{rad} will reach the pool, thereby contributing to the energy balance of the LM in the EC. Conversely, the remaining fraction $(1 - f_{rad,pool})$ of Q_{rad} , which in the schematic is called $Q_{rad,walls}$, represents a source term for the energy balance of the walls;
- $Q_{repl}(W)$ is the heat load associated to the LM replenished to the pool;
- $Q_{pool \rightarrow wall}(W)$ is the amount of heat lost from the LM pool to the underlying structures. It is evaluated by assuming only heat conduction to be relevant in the pool:

$$Q_{pool \rightarrow wall} = 2\pi \int_{A_{pool \rightarrow wall}} R h_{pool}(T_{pool} - T_{wall}) dA \quad (2)$$

Where:

- $A_{pool \rightarrow wall}$ (m^2) is the contact area between pool and wall;
- R is the radial coordinate;
- $h_{pool}(W/(m^2K)) \sim \frac{k_{pool}}{s_{pool}}$ is the equivalent heat transfer coefficient due to thermal conduction;
- T_{pool} is the pool temperature;

- T_{wall} is the temperature distribution over the surfaces of the box structures which are in contact with the LM pool.

The relevant engineering outcomes of this module are:

- The LM pool temperature;
- The vapor outflow towards the main plasma chamber;
- The amount of recirculated mass flow rate.

One shortcoming of the model is that, being 0D in nature, it is incapable of capturing the hotspot temperature of the walls below the LM pool.

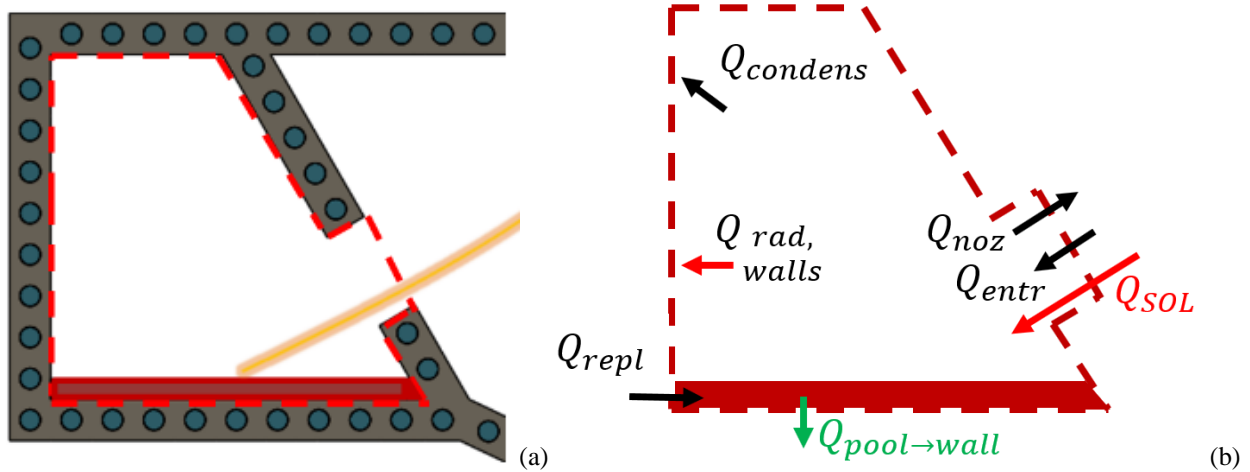


Figure 6. Schematic of the energy balance of the LM in the EC

This thermodynamic model is strictly applicable only if the vapor is in the continuum regime. However, as back-of-the-envelope estimations of the vapor Knudsen number in the chambers have shown (see [45]), this may not be the case, especially in the DC. We have therefore benchmarked the 0D model against a 2D kinetic model, see Appendix A. The results of the benchmark are encouraging, showing that the 0D model can be used to provide fast results which are semi-quantitatively correct.

5.2. 2D model of the walls

To determine the wall temperature distribution based on the heat load on walls, on the geometry and on the coolant temperature and assumed heat transfer coefficient, we solve the heat equation in the domain of the box walls.

The boundary conditions for the model are as follows:

- Outer walls are adiabatic (heat exhaust only occurs via the cooling channels);
- The heat transfer at the interface between pool and wall $Q_{pool \rightarrow wall}$ is modeled with an equivalent heat transfer coefficient h_{pool} , as already mentioned;
- The heat load on the walls which are not in contact with the LM pool is the sum of $Q_{condens}$ and $Q_{rad,walls}$. The corresponding heat flux (in W/m^2) to be provided to the 2D model of the walls is evaluated by dividing $Q_{condens}$ and $Q_{rad,walls}$ by the surface area available for condensation and radiation, respectively, thereby obtaining $q''_{condens}$ and $q''_{rad,walls}$. This means that the actual distribution of the load on the chamber walls is neglected for the time being;
- The active cooling is characterized by a coolant temperature $T_{coolant}$ and a heat transfer coefficient h .

A schematic of the boundary conditions is provided, for the IEC, in Figure 7. In the schematic $q'' = q''_{rad,walls} + q''_{condens}$.

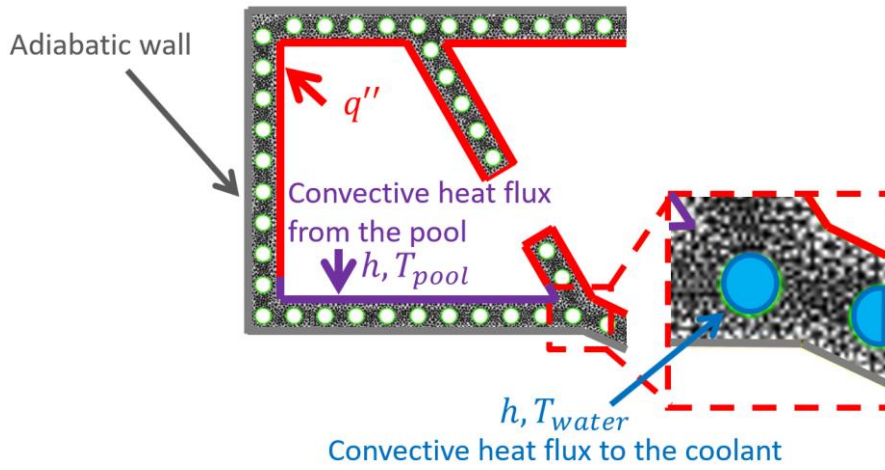


Figure 7. Schematic of the 2D FEM model

This module has been implemented in FreeFem++ [46].

5.3. 1D SOL model

In order to provide a description of the plasma parameters along the field lines while avoiding the excessively long computational times associated to 2D codes such as SOLPS a 1D modeling has been proposed. The adopted model has been derived by modifying the one proposed in [47]. Differently from the latter, we do not fix the target temperature, which is calculated as a result of the plasma power balance, and consider the plasma cooling due to the presence of vapor.

Figure 8 schematically represents the domain considered in the model. A single flux tube of width $\lambda_{q,OMP}$ is considered. Magnetic field lines expansion has been roughly taken into account by increasing the flux tube width by a factor f_{exp} at the divertor entrance (i.e. the location where the SOL plasma flowing towards the target along the field lines enters the ODC). It has been shown that the location chosen for this artificially localized flux expansion does not significantly affect the result [47]. Both inboard and outboard flux tubes are assumed to start at outboard midplane (OMP) and to extend up to the respective targets. However, it should be stressed that SOL plasma profiles evaluated with this approach for the inboard divertor leg are to be considered as purely qualitative, especially due to significant influence of drifts [47]. For this reason, we shall only show results for the outboard divertor leg.

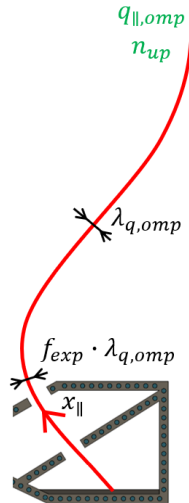


Figure 8. Schematic of the 1D SOL plasma model. The parallel-to-B coordinate $x_{||}$ is introduced (only the poloidal projection is shown).

Further simplifying assumptions are listed below:

1. Thanks to the fact that plasma temperature at target is not fixed, our approach can detect whether detachment conditions ([48]) will occur for a given scenario. However, in this case, we are not able to reconstruct the temperature and density profiles (the sheath heat transfer relation does not hold anymore, see eq. (8.2) below). Should detached conditions occur, we shall therefore assume that the entire parallel heat flux is radiated inside the EC;
2. Continuity, momentum and energy equations for the ionized vapor species are not considered, again for simplicity. The effect of vapor on hydrogenic plasma is simply associated to the local vapor density n_{vap} ;

3. A fixed particle dwell time τ along the SOL plasma is assumed, which is parametrically varied in order to assess the possible effects following from the non-coronal enhancement of the plasma cooling due to Li, which [21], [11] and other authors suggested to be relevant;
4. A single temperature for electrons and ions ($T_e = T_i = T$) is assumed.

In the following, the subscripts *TAR* and *OMP* indicate quantities at $x_{//} = 0$ (target) and $x_{//} = L$ (outboard midplane), respectively.

Continuity equation for the plasma:

$$\left\{ \begin{array}{l} \frac{d(nv)}{dx_{//}} = R_{iz}n_en_0 - R_{rec}n_en_i \\ v_{TAR} = -c_s(T_{TAR}) \end{array} \right. \quad (3.1)$$

$$(3.2)$$

The typical Bohm condition at the sheath edge is employed as a boundary condition, with c_s the sound speed. The resulting velocity v is negative due to the choice of the reference frame. Atomic data for H, i.e. reaction coefficients for ionization, recombination (and charge exchange, which will appear in the following equations) have been retrieved from the ADAS database [42]. The neutral density profile $n_0(x_{//})$ is considered fixed when solving this equation. A simple diffusive model for neutral transport has been employed for evaluating the neutral density n_0 , taking into account ionization, recombination, charge-exchange and recycling from target. This model is not discussed here since it is essentially the same as the one proposed in [47], which can be regarded as a reference.

Momentum conservation for the plasma:

$$\left\{ \begin{array}{l} \frac{d[n(m_iv^2 + 2eT)]}{dx_{//}} = -m_ivR_{CX}n_in_0 - m_ivR_{rec}n_en_i \\ n_{OMP} = 0.00236\langle n_e \rangle k^{1.11} B_\phi^{0.78} \end{array} \right. \quad (4.1)$$

$$(4.2)$$

Momentum is lost due to CX with neutrals and recombination. As suggested in [47], a possible momentum source associated to ionization is neglected, as well as ion-neutral friction. Solution to this equation provides the plasma density n .

The adopted boundary condition was proposed in [49] to relate the upstream SOL plasma density n_{OMP} to the average core plasma density $\langle n_e \rangle$. In this relation, k is the plasma elongation and B_ϕ the toroidal component of the magnetic field at OMP.

Energy conservation for the plasma:

$$\left\{ \begin{array}{l} \frac{dq_{//}}{dx_{//}} = -L_z(T_e, n_e \tau) n_e n_{vap} - eT_i R_{CX}(T_i, n_e) n_i n_0 - eE_{iz} R_{iz}(T_e, n_e) n_e n_0 \\ q_{//}(x_{//} = L) = q_{//,OMP} \end{array} \right. \quad (5.1)$$

$$(5.2)$$

where:

- $q_{//}$ is the total parallel heat flux, i.e. the sum of the heat fluxes transported via conduction and via convection;

$$q_{//} = q_{//,cond} + q_{//,conv} \quad (6)$$

- L_z is the cooling function associated to plasma-vapor interactions;
- n_{vap} is the vapor density, which is a result of the OD thermodynamic model;
- R_{CX} is the charge-exchange rate coefficient;
- R_{iz} is the ionization rate coefficient;
- E_{iz} is the ionization potential of H.

The three loss terms, which lead to a progressive reduction of the total parallel heat flux, are in turn plasma cooling mechanisms due to plasma-vapor interactions, charge-exchange of neutrals and ionization of neutrals. It is expected that the last two terms will only be relevant very close to the target, where the neutral density is high. Hydrogen radiation has been neglected, as this contribution is expected to be several orders of magnitude weaker than the other contributions to the plasma energy balance [47].

The upstream parallel heat flux $q_{//,OMP}$ has been evaluated by dividing the upstream power by the cross-sectional area of the plasma flux bundle [3].

$$q_{//,OMP} = \frac{P_{up}}{2\pi R_{OMP} \lambda_{q,OMP} \left(\frac{B_\theta}{|B|}\right)_{OMP}} \quad (7)$$

Where B is the total magnetic field, B_θ is its poloidal component and $\lambda_{q,OMP}$ has been evaluated according to [30]. To take into account flux expansion, at a distance from the target $x_{//} = L_{EC} + L_{DC} = L_{DIV}$ the heat flux is reduced by a factor f_{exp} .

To evaluate the plasma temperature, we employ the Fourier relation:

$$\begin{cases} q_{//,cond} = -k_0 T_e^{5/2} \frac{dT}{dx_{//}} & (8.1) \\ T(x_{//} = 0) = \frac{q_{//,TAR}}{\gamma_{se} \cdot e \cdot \Gamma_{se}} & (8.2) \end{cases}$$

where $k_0 \sim 2390 \frac{W}{m \cdot eV^{7/2}}$ and the boundary condition (6.2) is given by the sheath heat transfer relation ($\gamma_{se}=7$ is the sheath heat transfer coefficient [49]). Since equation (4) provides the distribution of $q_{//}$, to obtain $q_{//,cond}$ from it, it is necessary to subtract the convective contribution $q_{//,conv}$, given by

$$q_{//,conv} = \left(5eTn + \frac{1}{2} m_i n v^2\right) v \quad (9)$$

which is obviously more relevant close to the target due to the increase of the plasma flow speed.

As a final remark, we point out the fact that, since ionized species are not followed by the model (see assumption 2.) the location where the ionized vapor recombines is not known. This location is interesting, as power committed to ionization is released where recombination of the Li plasma occurs (i.e. in the bulk or at target). In our calculations we assume volumetric recombination to occur in the EC, before reaching the target, as suggested in [21].

6. Model input for the application to the DTT

Table 2 summarizes the input data assumed for the calculation, together with the corresponding reference. The machine parameters are consistent with the reference DTT scenario as indicated in [26]. Simulations considering Li and Sn as LM only differ for the LM thermophysical and atomic properties. For Li, two different values of the particle dwell time τ are considered, namely $\tau_1 = 1 \text{ ms}$ and $\tau_2 = 10 \text{ ms}$. For Sn, instead, results for $\tau = \infty$ (coronal equilibrium) will be presented, due to the much weaker dependence of the cooling function on τ , which is evident from Figure 4. The recycling coefficient at the target is assumed to be equal to 1 in all cases. As stated above, indeed, the Li surface is verified a posteriori to be too hot to retain H. For the sake of simplicity, Sn is assumed not to retain H significantly, since detailed experimental studies are still ongoing [50]. Again for the sake of simplicity, the fraction of radiated power which is directed towards the pool is evaluated as

$$f_{rad,pool} \sim \frac{A_{pool}}{A_{pool} + A_{walls,EC}} \quad (10)$$

Table 2. Machine and geometric inputs

Quantity (units)	Value	Meaning	Ref.
$P_{SOL,outboard}$ (MW)	21.3	Power leaving the separatrix along the outboard divertor leg	[26]
$\lambda_{SOL,OMP}$ (mm)	2.1	Scrape/off layer thickness at the outboard midplane	Calculated based on [30]
$A_{ ,OMP}$ (m ²)	6.14E-3	Cross sectional area of flux bundle	Calculated
$q_{//,up,outboard}$ (GW/m ²)	2.2	Upstream parallel heat flux, outboard divertor leg	Calculated
$\langle n_e \rangle$ (m ⁻³)	1.7E20	Average core plasma density	[26]
n_{OMP} (m ⁻³)	1.2E20	Upstream SOL plasma density	Calculated based on [49]
M_{TAR}	1	Mach number at the targets	[49]
γ_{se}	7	Sheath heat transfer coefficient	[49]
Z_{eff}	1.2	Effective plasma atomic number	[26]
f_{exp}	3	Flux expansion factor	[25]
R	1	Recycling coefficient at the targets	See text
$f_{rad,pool}$	0.169	Fraction of radiated power towards the LM pool	See text

τ (ms)	$\tau_1 = 1$ $\tau_2 = 10$	Impurity particle dwell time in the SOL (only used for Li)	[22]
$L_{connection}$ (m)	18.9	Connection length	Calculated
$L_{//,ECI}$ (m)	0.52	Distance travelled by the plasma along the field lines within the various chambers	From CAD
$L_{//,ECO}$ (m)	0.58		
$L_{//,DCI}$ (m)	1.25		
$L_{//,DCO}$ (m)	1.31		

The parameters for the active cooling of the walls retained here are summarized in Table 3.

Table 3. Parameters for the active cooling

Quantity (unit)	value	Meaning
$T_{coolant}$ (°C)	120	Coolant inlet temperature
$h_{ECI}, h_{ECO}, h_{DCI}, h_{DCO}$ (W/m ² K)	5000	Heat transfer coefficient for cooling channels for the various chambers (assumed to be equal)

7. Results

In the following sections the results of the model are shown, comparing the cases of the two liquid metals selected for this study. First, the SOL plasma profiles are shown, to assess the influence of different LMs. Particular attention has been devoted to quantify the uncertainties associated to the use of a fixed value of τ throughout the SOL. Then the effect of the power exhaust on the LM and wall temperatures is shown. Finally, an estimate of the mass flow rates circulating in the system is provided.

7.1. 1D SOL plasma profiles

In this section a comparison between Li and Sn will be presented in terms of SOL plasma profiles for the outboard divertor leg.

The extent of the plasma cooling due to interactions with evaporated metal atoms is given by q_{cool} , as defined in eq. (1). The calculated spatial profile of this quantity along $x_{//}$ (a coordinate parallel to \mathbf{B} starting from the target) is shown in Figure 9. The discontinuity at $x_{//} = L_{//,OEC} \sim 0.6$ m is due to the corresponding discontinuity in $n_{vap}(x_{//})$ (see Figure 10) which is a consequence of the 0D model employed for describing the Li vapor, which evaluates a single density for each chamber. It can be noticed that the power lost by the plasma per unit volume $q_{cool}(x_{//})$ in the EC is similar in the case Sn, $\tau = \infty$ and in the case Li, τ_1 . As n_{vap} differs by \sim three orders of magnitude, this can be explained by looking at the cooling function L_Z , see Figure 11, since the electron density is similar among the three cases, see Figure 12. Indeed, we find that in the OEC the electron density is similar, and the three orders of magnitude difference between the loss functions are compensated by a three orders of magnitude difference between the vapor densities. This implies the fact that the SOL plasma response within the divertor region to the use of Sn is only slightly different with respect to the Li, τ_2 case.

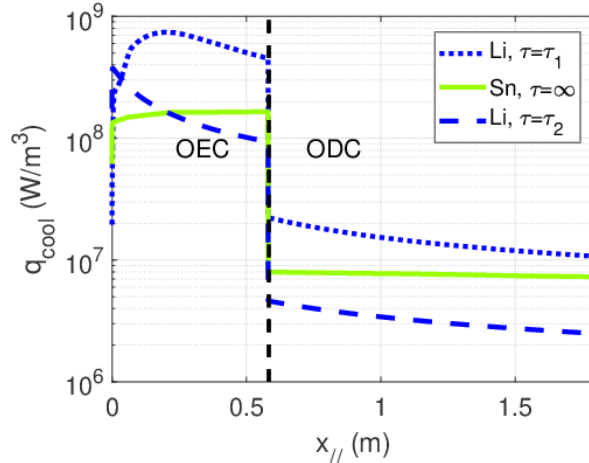


Figure 9. Parallel distribution of the power lost by the plasma per unit volume due to interactions with metal vapor in the outboard divertor region for Li (τ_1 and τ_2) and Sn ($\tau = \infty$). The $x_{//}$ coordinate runs parallel to \mathbf{B} , starting from the target ($x_{//} = 0$).

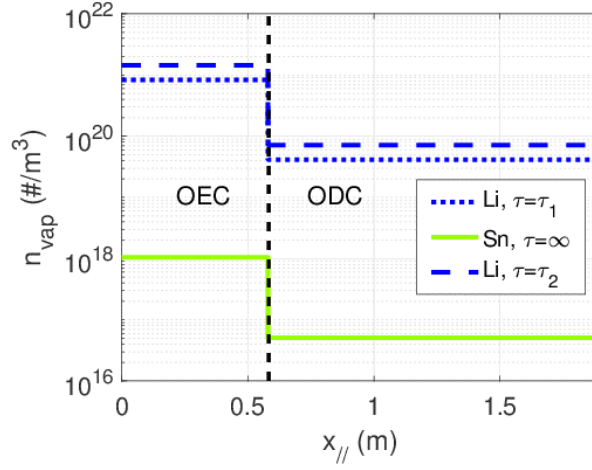


Figure 10. Parallel distribution of the metal vapor density in the outboard divertor region for Li (τ_1 and τ_2) and Sn ($\tau = \infty$). The $x_{||}$ coordinate runs parallel to B, starting from the target ($x_{||} = 0$).

Figure 11 shows the cooling function for the three cases considered here as a function of $x_{||}$. The value is plotted only in the divertor region since vapor density is assumed to be zero elsewhere. As expected from Figure 4, values for Sn are always several orders of magnitude larger than the ones for Li (for both τ_1 and τ_2). Note that, due to the strong non-linearity of the cooling function, a larger τ is not necessarily associated to a locally lower cooling function since the latter is strongly dependent also on the plasma temperature, see again Figure 4.

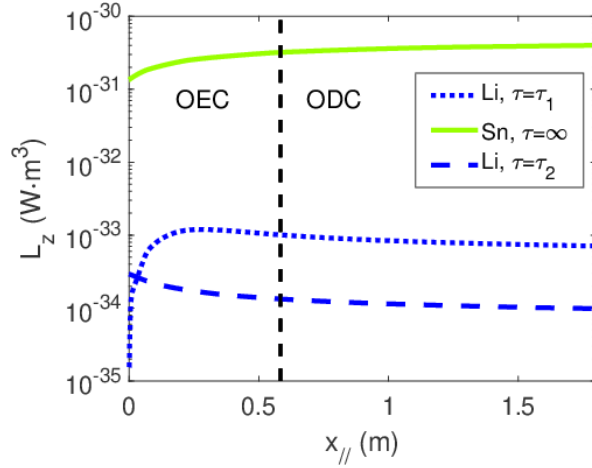


Figure 11. Parallel distribution of the cooling function in the outboard divertor region for Li (τ_1 and τ_2) and Sn ($\tau = \infty$). The $x_{||}$ coordinate runs parallel to B, starting from the target ($x_{||} = 0$).

Plasma density profiles are shown in Figure 12. The profiles for the three cases considered are comparable up to the entrance in the divertor region, then differences arise due to the different extent of plasma-vapor interactions. The case with Li, τ_1 corresponds to the lowest temperature (see Figure 13) and therefore to the highest density (due to total pressure conservation). Pressure conservation holds up to the point where plasma-neutral interactions become important. At this point, i.e. close to the target, the expected density peak associated to ionization of recycling neutrals is retrieved, which is larger for Li, τ_1 than for the other two cases. This is due to a stronger ionization source, $R_{iz} \cdot n_e \cdot n_0$, due to the different dependence of ionization rates on temperature and density. Finally, the usual density drop close to the target is associated to the flow acceleration up to $Mach = 1$ at the sheath edge.

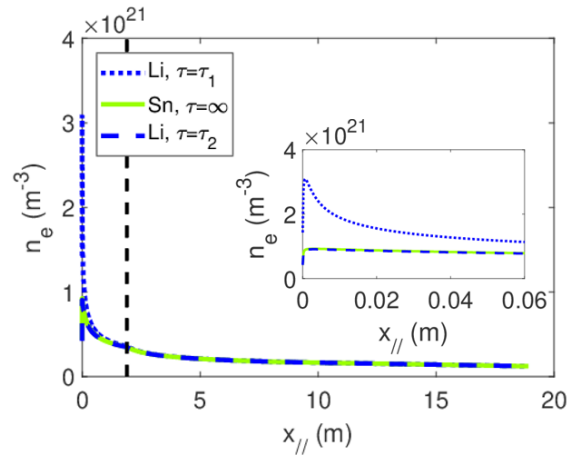


Figure 12. Parallel distribution of the plasma density in the outboard divertor region for Li (τ_1 and τ_2) and Sn. The vertical dashed line indicates $x_{||} = L_{||,DIV}$. The $x_{||}$ coordinate runs parallel to B, starting from the target ($x_{||} = 0$).

Finally, Figure 13 shows the computed temperature profiles. The general trend is consistent with expectations. The discontinuous first derivatives of the profiles at $x_{||} = L_{||,DIV} \sim 1.8$ m are due to the assumed localized flux expansion at the divertor entrance (the parallel heat flux suddenly decreases by a factor f_{exp} , and the temperature profile consequently flattens). After this point, i.e. for $x_{||} < L_{||,DIV}$, the flux bundle has entered the divertor region, where the energy loss term associated to plasma-vapor interactions becomes important. From Figure 13 it is evident that, for Li, the assumption of a larger value of τ implies a weaker plasma cooling effect and therefore a larger T_{TAR} , and globally a larger T_e within the divertor region. The final strong temperature drop close to $x_{||} = 0$ is associated to the plasma energy losses due to ionization of the neutrals, which locally overwhelms all other terms.

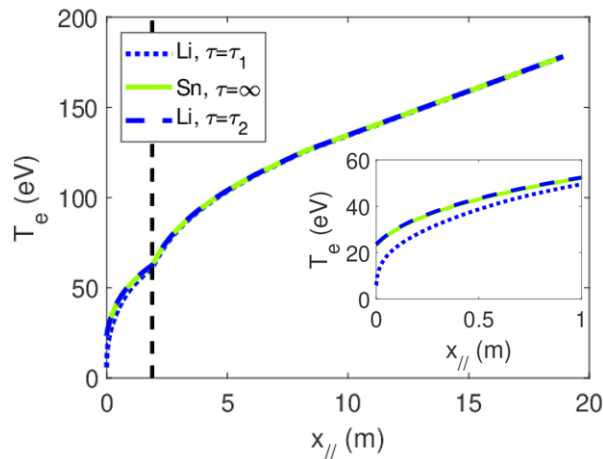


Figure 13. Parallel distribution of the plasma temperature in the outboard divertor region for Li (τ_1 and τ_2) and Sn. The vertical dashed line indicates $x_{||} = L_{||,DIV}$.

The results of this section show that the value of τ , which is one of the physical unknowns of the problem, indeed affects the plasma profiles in the case of Li. However, it is anticipated from Figure 9 that the thermodynamic state of the LM-vapor system is not much sensitive to this parameter (density of Li vapor n_z is similar for the cases τ_1 and τ_2). The following section shall further analyze this point, which is one of the most significant outcomes of the present work.

7.2. Vapor temperature

Figure 14 shows the temperatures evaluated in the divertor system for Li, $\tau = 1$ ms (a) and Sn (b). The temperature field over the structures evaluated by the 2D FEM model is shown, together with the value evaluated by the thermodynamic 0D model in each chamber. For clarity, the operating temperatures of the LM and vapor in both divertor chambers are shown in Figure 15.

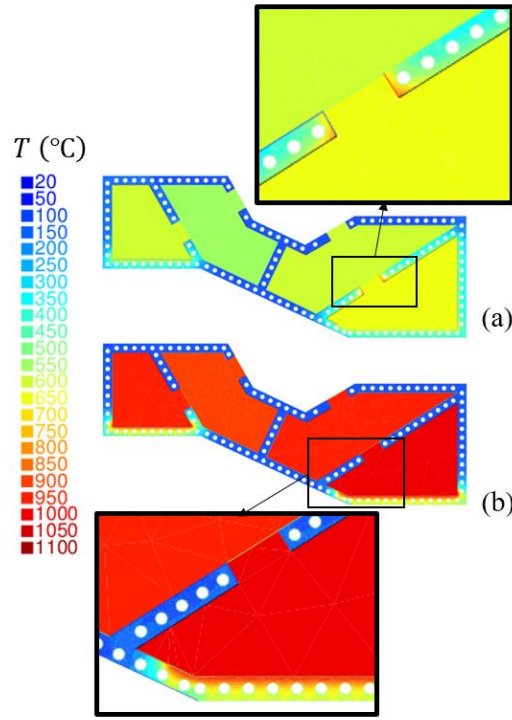


Figure 14. Temperature map of the structures and 0D temperature of the LM-vapor system in the ECs and of the vapor in the DCs for Li, τ_1 (a) and Sn (b)

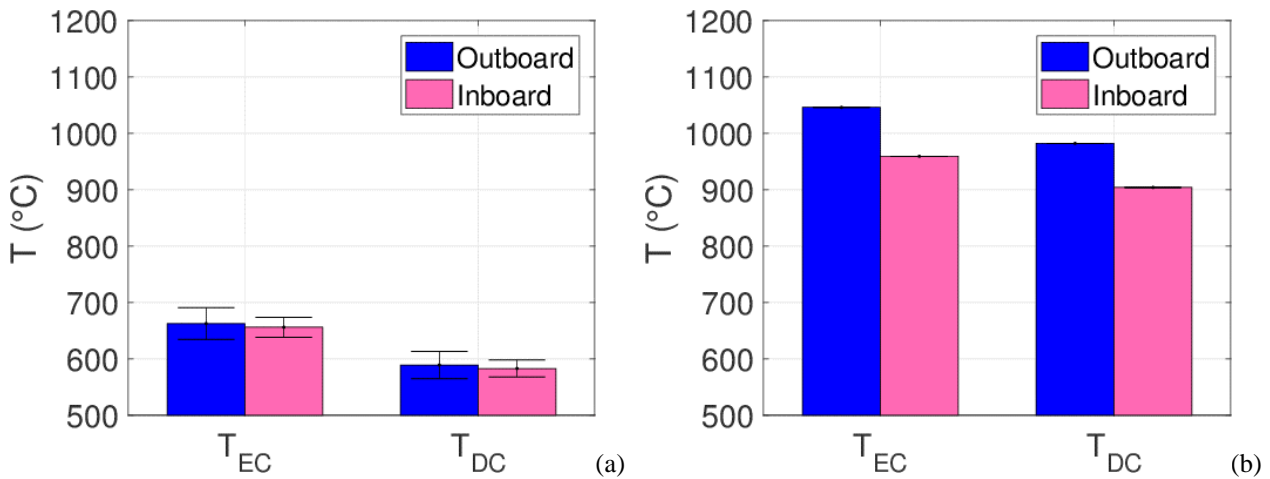


Figure 15. Temperatures of the LM-vapor system within the various chambers for Li (left) and Sn (right). Error bars account for uncertainty on τ (very small effect for Sn).

The significant difference between the two LMs is a consequence of the interplay between the many phenomena occurring and can be explained by looking at the power balance, which is detailed in Figure 16. All the terms appearing in Figure 6 are present, with the exception of Q_{entr} (which we assume to become part of Q_{rad}) and Q_{noz} , which in all cases represents a negligible contribution. It can be noticed that, for the case of Sn, the power actually reaching the pool, i.e. $Q_{pool \rightarrow wall}$, is larger. This occurs because the power entering the divertor is much less mitigated by radiation and evaporation/condensation with respect to the case of Li. As a consequence, a larger temperature is reached (the global heat transfer coefficient between the power deposition zone and the cooling channels for the two cases is indeed very similar, the only difference being associated to the pool thermal conductivity).

To justify the different power balance, a simple explanation is proposed: If no vapor was present, the only difference between the two LMs would be represented by their thermal conductivity, and therefore the different resistance offered by the pool to the flow of heat -of course, this is true since sputtering and consequent feedback on the plasma are neglected by this model. Since this difference is not significant, the system would reach a similar steady state temperature in the two cases, which is much larger than the temperatures actually foreseen by the model. Indeed, in the present case, if the target temperature is sufficiently large, evaporation occurs and partially accommodates for the unmitigated power by depositing it on walls thanks to condensation. Moreover, plasma cooling induced by the presence of a non-negligible amount of vapor in the chambers starts to take place. The temperature at which significant evaporation occurs is much lower for Li than for Sn (see again Figure 3), i.e. Sn is much more difficult to evaporate, and this explains why

$Q_{pool \rightarrow wall}^{Sn} > Q_{pool \rightarrow wall}^{Li}$ in Figure 16. In conclusion, a larger amount of heat will reach the pool unmitigated in the case of Sn.

Moreover, the difference between the distribution of the “mitigated” power between evaporation/condensation and radiation is due to the much larger values of the cooling function for Sn, with respect to Li, see Figure 4, even when the latter is far from coronal equilibrium. The amount of evaporated Sn is lower with respect to the amount of evaporated Li, and this explains the much lower condensation contribution. Nevertheless, the small amount of Sn present in the chambers is sufficient to radiate a not negligible amount of power (see again Figure 16). This is due to the much larger value of the cooling function, as it has been shown in Figure 4 and Figure 11.

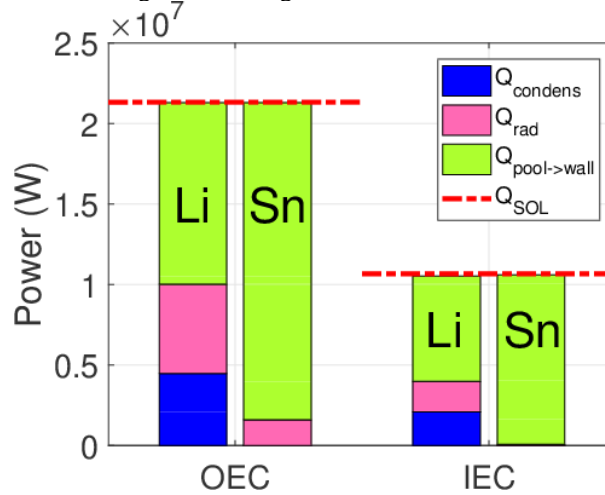


Figure 16. Power balance for Li, $\tau = 1$ ms and Sn

Similar arguments can be employed to explain the interesting result shown in Figure 17, where a parametric scan on τ is presented for Li. This histogram explains why, according to the present calculations, τ does not significantly affect the operating temperature of the system (see error bars in Figure 15) notwithstanding the large difference in radiated power (see again Figure 9). Indeed, the lower amount of power radiated in the case $\tau = 10$ ms implies a larger heat flux to the pool, which is almost totally accommodated by a more significant evaporation, thereby avoiding a large temperature increase (from Figure 3 it is clear that for Li at the temperatures considered here, a small temperature variation is sufficient to increase the evaporation rate by an order of magnitude).

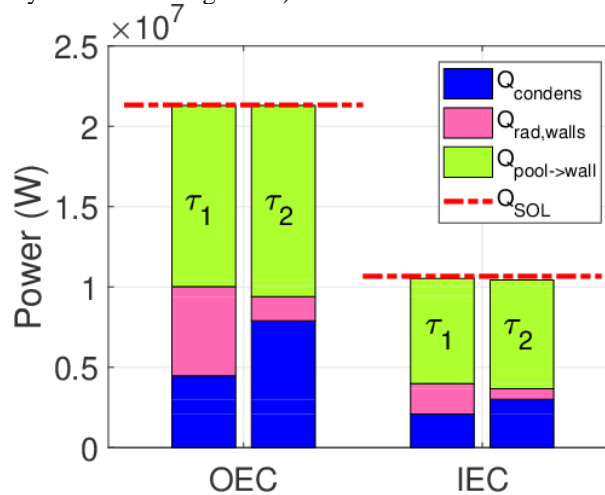


Figure 17. Power balance for Li, $\tau = 1$ ms and Li, $\tau = 10$ ms

A further comment concerning the power distribution is associated to the -relatively low- mitigation of the incoming power (~50% for Li, much lower for Sn). Even though a pool could in principle tolerate any value of incoming heat flux, the solid substrate of the pool might still reach unacceptable temperatures, e.g. from the point of view of the material compatibility. Heat load mitigation could be increased by designing a divertor with a larger $L_{//,DIV}$, the distance travelled by the plasma along the SOL within the divertor, which corresponds to the interaction length between the SOL plasma and the metal vapor confined in the box structure. However, in general this fact conflicts with the constraints of the plasma chamber. Another possibility would be to provide a worse cooling of the structures below the pool, with the effect of increasing the pool temperature and, consequently, the vapor density, to the expense of a larger vapor flow out of the DCs. The latter could at least partially be prevented by providing a better cooling of the DC walls.

7.3. Mass transport

Among the mass flow rates circulating in the system or flowing through the apertures, the most relevant ones are:

- the condensation mass flow rate within the EC $G_{condens,EC}$, i.e. the amount of LM “recirculating” within this chamber;
- the condensation mass flow rate within the DC $G_{condens,DC}$, which should be regarded as an input for the external purification loop;
- the amount of vapor escaping through the aperture of the DC towards the main plasma chamber $G_{DC \rightarrow MC}$. In the case of Li, this amount of LM might provide the beneficial effects already discussed on the plasma discharge. However, the maximum allowable $G_{DC \rightarrow MC}^{Li}$ is limited by fuel dilution. For Sn, this amount of vapor is instead harmful for the plasma purity and should therefore be kept as low as possible. Moreover, it should be kept in mind that in both cases a mechanism for collecting and finally recirculating also this mass of Li within the MC should be devised.

$G_{condens,EC}$, $G_{condens,DC}$, $G_{DC \rightarrow MC}$ are reported in Figure 18(a) for Li and Figure 18(b) for Sn. The results can provide an input for the design of the external LM recirculation/purification system and for an assessment of the acceptability of the flux of vapor to the MC, both in terms of plasma dilution/purity and in terms of material collection. The very big difference in $G_{DC \rightarrow MC}$ between Li and Sn could be deceptive, however, please consider that a much smaller influx of Sn than Li could cause comparable damage in the main plasma, so that, for a really quantitative and conclusive judgment of this comparison, these fluxes should be used as drivers of a calculation of the distribution of Z_{eff} and radiated power along the minor plasma radius as it could be performed, e.g., using the STRAHL code [51]. A feedback from these assessments could be employed for modifying the target cooling strategy (inlet coolant temperature, heat transfer coefficient, pool thickness).

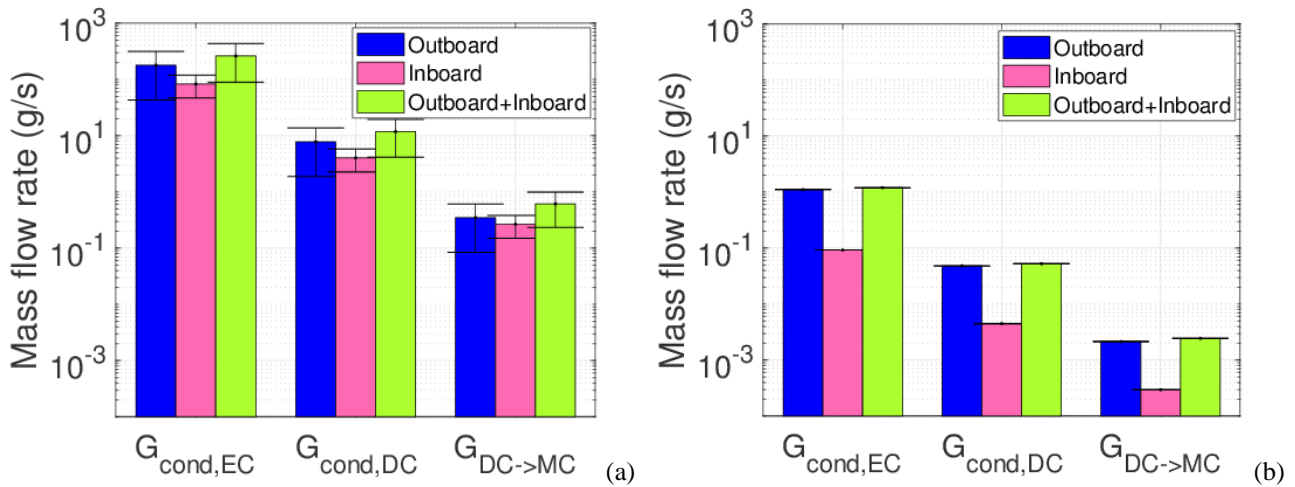


Figure 18. Mass flow rates of LM condensed in the divertor chambers and of vapor entering the MC as evaluated by the model for Li (a) and Sn (b). Error bars account for uncertainties on the parameter τ .

8. Conclusions

A self-consistent model for an LM vapor box divertor of pool type has been developed and applied to the case of the DTT, comparing Li and Sn as possible alternative LM choices.

For Li:

- both evaporation and radiation cooling are effective in reducing the target heat load.
- The maximum temperature of the target is evaluated around 700 °C, which is compatible with a W substrate [32].
- Further investigations are required to determine whether the amount of Li vapor flowing into the main plasma chamber is sufficiently low to avoid excessive plasma contamination.
- The condition of a significant amount of power exhausted via the “alternative” channels (i.e. radiation and evaporation/condensation), which is one of the main advantages of this type of divertor, can be already obtained with just two chambers. Should the amount of vapor flux towards the MC turn out to be too large, the number of chambers can be increased, retaining the same envelope, to provide a more effective differential pumping and hence further reduce this flux.

For Sn:

- a much less significant contribution of evaporation/condensation cooling has been evaluated. Indeed, according to the results presented in this paper, a very small density of Sn vapor is foreseen to be present in the system.
- This result implies that, at least for the configuration at hand, the vapor box concept, which is intended to confine a large density of vapor to exhaust plasma power by radiation+evaporation/condensation is not interesting.
- Nevertheless, we observe that the box structure is still useful to reduce the Sn vapor flow out towards the main plasma chamber by two orders of magnitude.

- Also in this case, further investigations are required to determine whether the amount of Sn vapor flowing into the main plasma chamber is sufficiently low.

The present study has identified several design parameters that could provide a more efficient operation of the proposed concept in terms of heat load spreading on the chamber wall surfaces, and namely:

- the heat transfer coefficient, or equivalently the coolant temperature within the cooling channels below the pool. Compatibly with other constraints, this could allow for a larger density of vapor to be confined in the EC, and a more effective load spreading;
- the interaction length between the plasma and the Li vapor, which should be increased, e.g. by considering a deeper position of the target. This might however not be compatible with the chamber geometry, which will be considered fixed when designing this system- in order to obtain a stronger cooling of the plasma.

The two parameters can be varied separately or together. The best strategy would be characterized by a sufficient Li vapor density to induce plasma detachment - promoted by *intrinsic*, rather than *extrinsic*, impurities- as already suggested in [52].

Acknowledgments

This work has been carried out within the framework of the EUROfusion Consortium and has received funding from the Euratom research and training programme 2014–2018 and 2019-2020 under grant agreement No 633053. The views and opinions expressed herein do not necessarily reflect those of the European Commission. We thank S. Carli for help with the comparison of the different atomic physics data bases available.

Appendix A. 2D Direct Simulation Monte Carlo (DSMC) approach for rarefied vapor modelling

A.1. DSMC motivation and simulation setup

The motivation for a detailed study of the vapor dynamics, as mentioned above, is that it has to be assessed whether the 0D treatment of the vapor discussed above can be applied even if the vapor is rarefied. If the assessment is successful, we can use the 0D model for fast calculations and parametric scans in the framework of the above-described self-consistent model. Moreover, developing a detailed model for the vapor can provide information concerning the actual distribution of the vapor within the chambers, which influences not only the plasma-vapor interactions but also the distribution of the condensate on the walls. Therefore, we propose here a 2D (axisymmetric) model for the vapor dynamic, which accounts for the actual divertor geometry and evaluates the distribution of the thermodynamic variables for the vapor inside the chambers. The model is based on the Direct Simulation Monte Carlo (DSMC) method (see [53] for a thorough introduction).

Simulations have been performed by means of the DSMC method implementation recently included in OpenFOAM [54], namely *dsmcFoamPlus* [55]. The OpenFOAM environment has been selected since it is modular and easily coupled to other codes. Moreover, being open-source, the program can be modified to include specific features of the system being studied.

Mesh generation and time step selection have been performed in compliance with the guidelines for the DSMC method ([53],[56]). In particular, the characteristic grid size should always be smaller than the local value of λ , in order to properly take into account inter-particle collisions. For a similar reason, the time step should be smaller than λ/\bar{u} , \bar{u} being the mean thermal speed. In [56] it is therefore recommended that $\Delta x \leq \lambda/3$ and $\Delta t \leq \lambda/(10\bar{u})$. Average values of T and n for each chamber from the foregoing 0D calculations are employed to estimate the required Δx in each chamber -to be set as a criterion for the mesh generation- and Δt . As a result, a coarser mesh is employed in the DC ($\Delta x \sim 0.3$ mm) than in the EC ($\Delta x \sim 0.1$ mm), see Figure 19. The scaling factor, defined as the number of real particles that each DSMC particle represents, is evaluated as:

$$f = \frac{(\Delta x)^2 n}{NPC} \quad (13)$$

Where NPC is the average number of particles per cell. In our simulations, Δx is further adjusted in order to have $f = 10^{12}$ with an average value of NPC of 50 [53],[56].

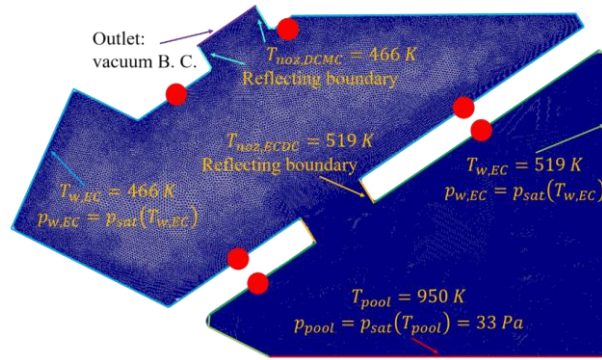


Figure 19. Schematic of the simulation domain, including mesh and boundary conditions. Red dots indicate boundaries which are considered as condensing in Case 1 and reflecting in Case 2.

To provide a significant benchmark for the OD calculations above, consistent boundary conditions must be enforced. Boundary conditions are indicated in Figure 19 and explained in the following.

- (a) LM pool: the pool represents the bottom boundary for the vapor domain. A single temperature for the entire pool is imposed, together with a pressure corresponding to the saturation pressure at that temperature. The effect of specifying the temperature is to fix the mean speed of the Maxwellian distribution according to which evaporated particles are emitted. Specifying the pressure imposes instead the number of particles emitted -the larger the pressure, the larger the number of particles which must be emitted to maintain this pressure in the cells adjacent to the pool.
- (b) Chamber walls: the walls are classified according to the comparison between the local wall temperature T_w and the local saturation temperature T_{vap} .

1. If $T_w < T_{vap}$, the wall is condensing. In this condition, the walls are assumed to be covered by a layer (or film) of condensed LM. The LM layer is assumed to be thin, so that the temperature of the liquid-vapor interface (which corresponds to the boundary of the vapor domain) can be assumed equal to the inner wall temperature. In this condition, all particles hitting the wall (i.e. the film) are absorbed, whereas a number of particles which is consistent with the local wall interface temperature and saturation pressure is emitted. Clearly, for a condensing wall the net effect of this combination of evaporation/condensation is shifted towards condensation, i.e. the boundary is absorbing particles;
2. If $T_w > T_{vap}$, the wall is reflecting. In this condition, no LM film can be present on the wall, and the boundary of the vapor domain corresponds to the wall itself. The reflection is assumed to be diffuse, i.e. particles hitting this boundary are reflected with a velocity distribution corresponding to a Maxwellian at the local wall temperature.

These specifications are the equivalent, from a molecular point of view, of the Hertz-Knudsen equation which has been employed for the OD model. In this work, as shown in Figure 19, the wall temperature is imposed and the local condensing or reflecting behavior is evaluated accordingly.

- (c) Nozzle walls: these surfaces are assumed to be reflecting, regardless of their temperature.
- (d) Chamber walls marked by a red dot in Fig. 3, and nozzle walls: for these walls two cases are considered.
 1. *Case 1*: the condensing behavior of the walls is according to point (b1);
 2. *Case 2*: the walls are forced to be reflecting, independently of their temperature.

In particular, *Case 1* is intended to benchmark the results of the OD model, whereas *Case 2* is intended to show the capabilities of the proposed approach to drive design choices for the system under study.

- (e) Aperture towards the MC: since a very small quantity of Li is expected to be present in the MC, a vacuum boundary condition is employed (i.e. all particles hitting this boundary are absorbed, and no particle is re-emitted).

A.2. DSMC results and discussion

Steady state results for the reference scenario described above are presented in this section. Figure 20 shows the calculated Mach number map with the corresponding streamlines in the two cases. In both cases, the vapor expands from the boundary at the largest pressure -i.e. the pool- towards, eventually, the perfect vacuum assumed at outlet. The situation is close to a free expansion, since condensing surfaces behave almost as perfect absorbers. The presence of reflecting surfaces -i.e. the nozzles in both Case 1 and Case 2, and the surfaces with a red dot in Case 2- deviates and slows down the flow, possibly causing shocks when the flow speed is reduced from supersonic to subsonic. This fact is particularly evident for Case 2, where a clear shock front is produced in the DC.

Figure 21 shows the 2D Li vapor density map for both Case 1 (left) and Case 2 (right). In Case 2, a density larger by a factor ~ 2 is achieved in the EC thanks to the presence of reflecting surfaces normal to the flow direction. This is desirable if plasma cooling associated to interactions with the vapor is to be maximized, as the extent of these interactions is directly proportional to the density of the neutral Li encountered by the plasma along its path towards the target. Nevertheless,

the reduced area available for condensation results in an amount of Li which flows out of the system towards the MC larger by a factor ~ 1.3 . A conclusion concerning the best available option is not straightforward, since it would require detailed information concerning the core plasma compatibility of the leaked Li vapor and the actual benefits of a reduced heat load on the pool. Nevertheless, it can be stated that reflecting surfaces are only interesting in the EC, where they increase the vapor density, but are not desirable in the DC, where the main interest is to maximize the vapor condensation.

1D plots shown in Figure 22 finally allow to carry out the desired benchmark against 0D and 2D results, and to compare features of Case 1 and Case 2. The left plot shows a difference lower than a factor ~ 2 between the density evaluated by the 0D and the 2D model. Nevertheless, the 0D model is conservative, in that it calculates a lower density, therefore lower plasma-vapor interactions and therefore a larger plasma load on the pool. Again, it is clear that Case 2 provides a more uniform density in the EC, which is desirable for enhancing plasma cooling. The right plot shows instead that temperature is overpredicted in the EC -and, consequently, in the DC- by the 0D model, due to the fact that:

- Vapor in the EC is assumed to be at saturation conditions corresponding to the pool temperature, which is not strictly correct due to the fact that the vapor is in contact with walls colder than the pool in the EC;
- Supersonic vapor expansion occurring already in the EC is neglected.

We conclude from this analysis that the 0D model is suitable for the purpose of being coupled with the plasma model and the model of the walls, as it provides an adequate estimate of the vapor density within the chambers.

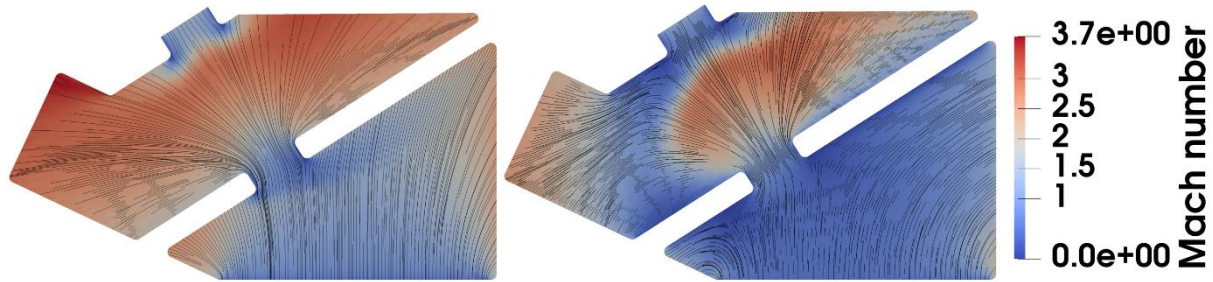


Figure 20. Computed Mach number map with streamlines in Case 1 (left) and Case 2 (right)

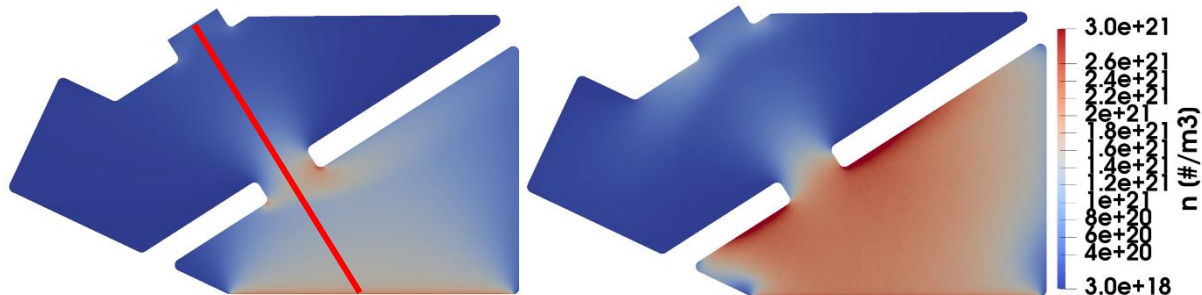


Figure 21. Density map of the Li vapor in Case 1 (left) with indication of the probe line employed for producing 1D plots, and Case 2 (right)

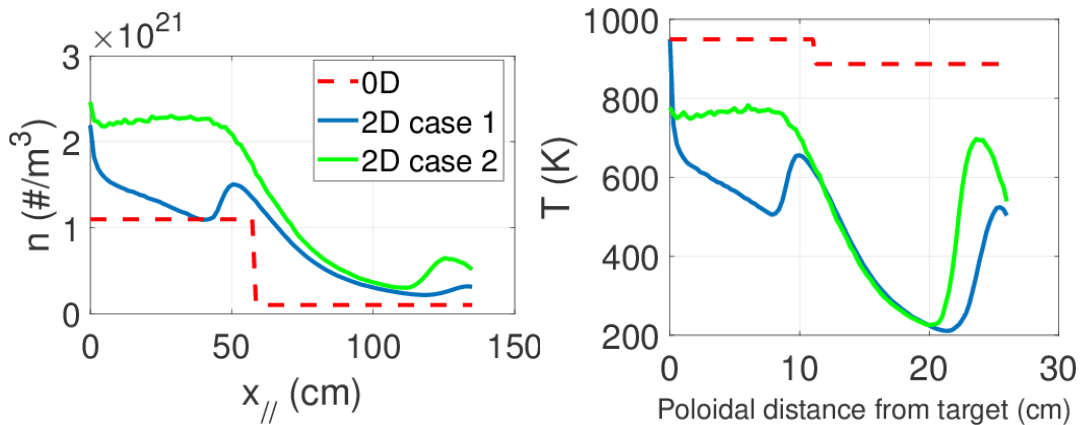


Figure 22. Calculated vapor density (left) and temperature (right) evaluated along the probe line by the 0D model (red dotted line) and by the 2D DSMC model for Case 1 (solid blue line) and Case 2 (solid green line). Note that the x coordinate for the density corresponds to the distance from the pool, evaluated along a magnetic field line.

References

- [1] EUROfusion, “European Research Roadmap to the Realisation of Fusion Energy,” 2018.
- [2] L. G. Golubchikov, V. A. Evtikhin, I. E. Lyublinski, V. I. Pistunovich, I. N. Potapov, and A. N. Chumanov, “Development of a liquid-metal fusion reactor divertor with a capillary-pore system,” *J. Nucl. Mater.*, vol. 233, pp. 667–672, 1996.
- [3] V. A. Evtikhin, I. E. Lyublinski, A. V. Vertkov, V. G. Belan, I. K. Konkashbaev, and L. B. Nikandrov, “Calculation and experimental investigation of fusion reactor divertor plate and first wall protection by capillary-pore systems with lithium,” *J. Nucl. Mater.*, vol. 271–272, pp. 396–400, 1999.
- [4] M. J. Baldwin, R. P. Doerner, S. C. Luckhardt, and R. W. Conn, “Deuterium retention in liquid lithium,” *Nucl. Fusion*, vol. 42, no. 11, pp. 1318–1323, 2002.
- [5] M. A. Jaworski, N. B. Morley, and D. N. Ruzic, “Thermocapillary and thermoelectric effects in liquid lithium plasma facing components,” *J. Nucl. Mater.*, vol. 390–391, no. 1, pp. 1055–1058, 2009.
- [6] M. A. Jaworski *et al.*, “Upgrades toward high-heat flux, liquid lithium plasma-facing components in the NSTX-U,” *Fusion Eng. Des.*, vol. 112, pp. 93–101, 2016.
- [7] H. W. Kugel *et al.*, “NSTX plasma operation with a Liquid Lithium Divertor,” *Fusion Eng. Des.*, vol. 87, no. 10, pp. 1724–1731, 2012.
- [8] R. Kaita *et al.*, “Hydrogen retention in lithium on metallic walls from ‘in vacuo’ analysis in LTX and implications for high-Z plasma-facing components in NSTX-U,” *Fusion Eng. Des.*, vol. 117, pp. 135–139, 2017.
- [9] M. Y. Zharkov, A. V. Vertkov, I. E. Lyublinski, S. V. Mirnov, V. B. Lazarev, and A. N. Szherbak, “Development of lithium CPS based limiters for realization of a concept of closed lithium circulation loop in Tokamak,” *Phys. Procedia*, vol. 71, no. February, pp. 47–51, 2015.
- [10] G. Mazzitelli, M. L. Apicella, and A. Alexeyev, “Heat loads on FTU liquid lithium limiter,” *Fusion Eng. Des.*, vol. 86, no. 6–8, pp. 580–583, 2011.
- [11] S. Mirnov, “Plasma-wall interactions and plasma behaviour in fusion devices with liquid lithium plasma facing components,” *J. Nucl. Mater.*, vol. 390–391, no. 1, pp. 876–885, 2009.
- [12] V. A. Evtikhin *et al.*, “Lithium divertor concept and results of supporting experiments,” *Plasma Phys. Control. Fusion*, vol. 44, no. 6, pp. 955–977, 2002.
- [13] P. Rindt, T. W. Morgan, M. A. Jaworski, and N. J. Lopes Cardozo, “Power handling limit of liquid lithium divertor targets,” *Nucl. Fusion*, vol. 58, no. 10, p. 104002 (5 pp), 2018.
- [14] R. A. Pitts *et al.*, “Physics conclusions in support of ITER W divertor monoblock shaping,” *Nucl. Mater. Energy*, vol. 12, pp. 60–74, Aug. 2017.
- [15] D. N. Ruzic, W. Xu, D. Andruczyk, and M. A. Jaworski, “Lithium-metal infused trenches (LiMIT) for heat removal in fusion devices,” *Nucl. Fusion*, vol. 51, no. 10, 2011.
- [16] M. Shimada and Y. Hirooka, “Actively convected liquid metal divertor,” *Nucl. Fusion*, vol. 54, p. 122002 (7 pp.), 2014.
- [17] F. L. Tabarés, E. Oyarzabal, A. B. Martin-Rojo, D. Tafalla, A. de Castro, and A. Soletto, “Reactor plasma facing component designs based on liquid metal concepts supported in porous systems,” *Nucl. Fusion*, vol. 57, p. 016029 (11 pp), 2017.
- [18] P. Fflis *et al.*, “Flowing liquid lithium plasma-facing components – Physics, technology and system analysis of the LiMIT system,” *Nucl. Mater. Energy*, vol. 12, pp. 1324–1329, Aug. 2017.
- [19] Y. Nagayama, “Liquid lithium divertor system for fusion reactor,” *Fusion Eng. Des.*, vol. 84, no. 7–11, pp. 1380–1383, 2009.
- [20] M. Ono, M. A. Jaworski, R. Kaita, Y. Hirooka, D. Andruczyk, and T. K. Gray, “Active radiative liquid lithium divertor concept,” *Fusion Eng. Des.*, vol. 89, no. 12, pp. 2838–2844, 2014.
- [21] R. J. Goldston, R. Myers, and J. Schwartz, “The lithium vapor box divertor,” *Phys. Scr.*, vol. 2016, no. T167, p. 14017, 2016.
- [22] R. J. Goldston, A. Hakim, G. W. Hammett, M. A. Jaworski, and J. Schwartz, “Recent advances towards a lithium vapor box divertor,” *Nucl. Mater. Energy*, vol. 12, pp. 1118–1121, Aug. 2017.
- [23] G. F. Nallo *et al.*, “Modeling the lithium loop in a liquid metal pool-type divertor,” *Fusion Eng. Des.*, vol. 125, pp. 206–215, Dec. 2017.
- [24] T. W. Morgan, P. Rindt, G. G. Van Eden, V. Kvon, M. A. Jaworski, and N. J. Lopes Cardozo, “Liquid metals as a divertor plasma facing material explored using the Pilot-PSI and Magnum- PSI linear devices,” *Plasma Phys. Control. Fusion*, vol. 60, no. 1, p. 014025 (11pp), 2018.
- [25] ENEA, *Divertor Tokamak Test facility Project Proposal*. 2015.
- [26] R. Albanese, “DTT: a divertor tokamak test facility for the study of the power exhaust issues in view of DEMO,” *Nucl. Fusion*, vol. 57, no. 1, p. 016010, 2017.
- [27] G. Maddaluno, D. Marzullo, G. Mazzitelli, S. Roccella, G. Di Gironimo, and R. Zanino, “The DTT device: Divertor solutions for alternative configurations including liquid metals,” *Fusion Eng. Des.*, vol. 122, pp. 341–348, 2017.
- [28] G. Di Gironimo, “Private communication.” 2017.
- [29] A. A. Pshenov and A. S. Kukushkin, “SOLPS4 . 3 Modeling of Lithium Transport and Noncoronal Radiation in

- the T-15 Tokamak with Lithium Emitter – Collector Scheme in Use 1,” vol. 44, no. 7, pp. 641–651, 2018.
- [30] R. J. Goldston, “Heuristic drift-based model of the power scrape-off width in low-gas-puff H-mode tokamaks,” *Nucl. Fusion*, vol. 52, no. 1, p. 013009 (7 pp), 2012.
- [31] C. Bachmann, “Requirements for a Liquid Metal Target based on Capillary Porous System in DEMO,” *Presented at Liquid Metal Target Workshop*. Prague, 2017.
- [32] A. Vertkov *et al.*, “The concept of lithium based plasma facing elements for steady state fusion tokamak-reactor and its experimental validation,” *Preprint: 2018 IAEA Fusion Energy Conference, Gandhinagar, EX/P1-12*. 2018.
- [33] J. W. Coenen *et al.*, “Liquid metals as alternative solution for the power exhaust of future fusion devices: Status and perspective,” *Phys. Scr.*, vol. T159, p. 014037 (7 pp.), 2014.
- [34] J. P. Allain, M. D. Coventry, and D. N. Ruzic, “Collisional and thermal effects on liquid lithium sputtering,” *Phys. Rev. B - Condens. Matter Mater. Phys.*, vol. 76, no. 20, pp. 1–12, 2007.
- [35] G. G. Van Eden, V. Kvon, M. C. M. Van De Sanden, and T. W. Morgan, “Oscillatory vapour shielding of liquid metal walls in nuclear fusion devices,” *Nat. Commun.*, vol. 8, no. 1, 2017.
- [36] R. J. Goldston, E. D. Emdee, M. A. Jaworski, M. E. Rensink, T. D. Rognlien, and J. A. Schwartz, “A simplified lithium vapor box divertor,” *Preprint: 2018 IAEA Fusion Energy Conference, Gandhinagar, FIP/3-6*. 2018.
- [37] M. Ono *et al.*, “Recent progress in the NSTX/NSTX-U lithium programme and prospects for reactor-relevant liquid-lithium based divertor development,” *Nucl. Fusion*, vol. 53, no. 11, 2013.
- [38] M. Ono *et al.*, “Implications of NSTX lithium results for magnetic fusion research,” *Fusion Eng. Des.*, vol. 85, pp. 882–889, 2010.
- [39] F. L. Tabares *et al.*, “Conference Report on the 4rd International Symposium on Lithium Applications,” *Nucl. Fusion*, vol. 56, p. 127002 (8 pp), 2016.
- [40] J. You, E. Visca, C. Bachmann, E. Divertor, and P. Team, “Critical issues & challenges in the engineering of DEMO divertor target,” 2015.
- [41] J. Safarian and T. A. Engh, “Vacuum Evaporation of Pure Metals,” *Metall. Mater. Trans. A*, vol. 44, no. 2, pp. 747–753, 2013.
- [42] H. P. Summers, “The ADAS User Manual, version 2.6,” 2004.
- [43] T. Putterich, E. Fable, R. Dux, R. Neu, M. G. O’Mullane, and R. Wenninger, “Impurity limits in a reactor grade fusion device,” in *42nd European Physical Society Conference on Plasma Physics, EPS 2015, paper n. 4.111*, 2015.
- [44] R. E. Nygren and F. L. Tabares, “Liquid surfaces for fusion plasma facing components—A critical review. Part I: Physics and PSI,” *Nucl. Mater. Energy*, vol. 9, pp. 6–21, 2016.
- [45] G. F. Nallo *et al.*, “Modeling the lithium loop in a liquid metal pool-type divertor,” *Fusion Eng. Des.*, vol. 125, pp. 206–215, 2017.
- [46] F. Hecht, “New development in freefem++,” *J. Numer. Math.*, vol. 20, no. 3–4, pp. 251–266, Jan. 2012.
- [47] A. Kallenbach, M. Bernert, R. Dux, F. Reimold, and M. Wischmeier, “Analytical calculations for impurity seeded partially detached divertor conditions,” *Plasma Phys. Control. Fusion*, vol. 58, no. 4, p. 45013, 2016.
- [48] A. A. Pshenov, A. S. Kukushkin, and S. I. Krasheninnikov, “Energy balance in plasma detachment,” *Nucl. Mater. Energy*, vol. 12, pp. 948–952, 2017.
- [49] P. C. Stangeby, “The Plasma Boundary of Magnetic Fusion Devices,” *Plasma Phys. Control. Fusion*, vol. 43, no. 2, pp. 223–224, 2001.
- [50] J. P. S. Loureiro *et al.*, “Deuterium retention in tin (Sn) and lithium–tin (Li–Sn) samples exposed to ISTTOK plasmas,” *Nucl. Mater. Energy*, vol. 12, pp. 709–713, 2017.
- [51] R. Dux, “STRAHL User Manual,” 2006.
- [52] R. J. Goldston, M. L. Reinke, and J. A. Schwartz, “A new scaling for divertor detachment,” *Plasma Phys. Control. Fusion*, vol. 59, no. 5, 2017.
- [53] G. A. Bird, *Molecular Gas Dynamics and the Direct Simulation of Gas Flows*. Oxford: Clarendon Press, 1994.
- [54] H. G. Weller, G. Tabor, C. Fureby, and H. Jasak, “A tensorial approach to computational continuum mechanics using object-oriented techniques,” *Comput. Phys.*, vol. 12, no. 6, pp. 620–631, 1998.
- [55] C. White *et al.*, “DsmcFoam+: An OpenFOAM based direct simulation Monte Carlo solver,” *Comput. Phys. Commun.*, vol. 224, pp. 22–43, 2017.
- [56] Z. X. Sun, Z. Tang, Y. L. He, and W. Q. Tao, “Proper cell dimension and number of particles per cell for DSMC,” *Comput. Fluids*, vol. 50, no. 1, pp. 1–9, 2011.